

Time-lapse three-dimensional inversion of complex conductivity data using an active time constrained (ATC) approach

M. Karaoulis, André Revil, D.D. Werkema, B.J. Minsley, W. F. Woodruff, A. Kemna

▶ **To cite this version:**

M. Karaoulis, André Revil, D.D. Werkema, B.J. Minsley, W. F. Woodruff, et al.. Time-lapse three-dimensional inversion of complex conductivity data using an active time constrained (ATC) approach. Geophysical Journal International, 2011, 187 (1), pp.237-251. 10.1111/j.1365-246X.2011.05156.x . insu-00680765

HAL Id: insu-00680765
https://insu.hal.science/insu-00680765

Submitted on 2 Mar 2021

HAL is a multi-disciplinary open access archive for the deposit and dissemination of scientific research documents, whether they are published or not. The documents may come from teaching and research institutions in France or abroad, or from public or private research centers.

L'archive ouverte pluridisciplinaire **HAL**, est destinée au dépôt et à la diffusion de documents scientifiques de niveau recherche, publiés ou non, émanant des établissements d'enseignement et de recherche français ou étrangers, des laboratoires publics ou privés.

Geophysical Journal International

Geophys. J. Int. (2011) **187,** 237–251 doi: 10.1111/j.1365-246X.2011.05156.x

Time-lapse three-dimensional inversion of complex conductivity data using an active time constrained (ATC) approach

M. Karaoulis,[1] A. Revil,[1,2] D. D. Werkema,[3] B. J. Minsley,[4] W. F. Woodruff[1] and A. Kemna[5]

[1] *Colorado School of Mines, Department of Geophysics, Golden, CO, USA. E-mail: arevil@mines.edu*
[2] *ISTerre, CNRS,* UMR 5559, *Université de Savoie, Equipe Volcan, Le Bourget du Lac, France*
[3] *U.S. EPA, ORD, NERL, ESD, CMB, Las Vegas, NV, USA*
[4] *USGS, Federal Center, Lakewood,* 10, CO 80225-0046, *USA*
[5] *Department of Geodynamics and Geophysics, University of Bonn, Nussallee* 8, Bonn 53115, *Germany*

Accepted 2011 July 14. Received 2011 July 13; in original form 2011 May 1

SUMMARY

Induced polarization (more precisely the magnitude and phase of impedance of the subsurface) is measured using a network of electrodes located at the ground surface or in boreholes. This method yields important information related to the distribution of permeability and contaminants in the shallow subsurface. We propose a new time-lapse 3-D modelling and inversion algorithm to image the evolution of complex conductivity over time. We discretize the subsurface using hexahedron cells. Each cell is assigned a complex resistivity or conductivity value. Using the finite-element approach, we model the in-phase and out-of-phase (quadrature) electrical potentials on the 3-D grid, which are then transformed into apparent complex resistivity. Inhomogeneous Dirichlet boundary conditions are used at the boundary of the domain. The calculation of the Jacobian matrix is based on the principles of reciprocity. The goal of time-lapse inversion is to determine the change in the complex resistivity of each cell of the spatial grid as a function of time. Each model along the time axis is called a 'reference space model'. This approach can be simplified into an inverse problem looking for the optimum of several reference space models using the approximation that the material properties vary linearly in time between two subsequent reference models. Regularizations in both space domain and time domain reduce inversion artefacts and improve the stability of the inversion problem. In addition, the use of the time-lapse equations allows the simultaneous inversion of data obtained at different times in just one inversion step (4-D inversion). The advantages of this new inversion algorithm are demonstrated on synthetic time-lapse data resulting from the simulation of a salt tracer test in a heterogeneous random material described by an anisotropic semi-variogram.

Key words: Electrical properties; Hydrogeophysics; Permeability and porosity.

GJI Marine geosciences and applied geophysics

Downloaded from https://academic.oup.com/gji/article/187/1/237/561878 by guest on 02 March 2021

1 INTRODUCTION

Electrical resistivity is sensitive to salinity, porosity, saturation, pore shape, temperature, clay content and biological activity (e.g. Waxman & Smits 1968; Revil *et al.* 1998; Atekwana *et al*. 2004). Variability in any of these parameters can have an influence on resistivity and can be monitored by time-lapse electrical resistivity tomography (TL-ERT). In the recent literature, TL-ERT has started to be a popular method to monitor dynamic processes occurring in the shallow subsurface (typically the first hundred metres, see Legaz *et al*. 2009; Müller *et al*. 2010, and references therein). The TL-ERT imaging, often involving permanent electrode installations, has proven to provide information complementary to *in situ* geochemical measurements. Applications of TL-ERT include monitoring of subsurface flow (e.g. Daily *et al*. 1992; Ramirez *et al*. 1993; Park 1998; Daily & Ramirez 2000; Nimmer *et al*. 2007), characterization of solute transport (e.g. Slater *et al*. 2000; Kemna *et al*. 2002; Singha & Gorelick 2005; Looms *et al*. 2008), saturation and temperature (Legaz *et al*. 2009) and mapping of salt-water intrusion in aquifers (e.g. Nguyen *et al*. 2009; Ogilvy *et al*. 2009), etc.

In an effort to extract more information about the subsurface geology (e.g. shale versus brine-saturated sands), the distribution of permeability and contaminants or to observe change in the precipitation of metallic particles (resulting from changes in the redox conditions) during bioremediation, resistivity measurements can

© 2011 The Authors
Geophysical Journal International © 2011 RAS

be extended in the frequency domain, typically in the range from 1 mHz to 1 kHz in the laboratory and 10 mHz to 100 Hz in the field (e.g. Olhoeft 1985, 1986; Börner *et al*. 1996; Vanhala 1997; Lesmes & Morgan 2001; Kemna *et al*. 2004; Nordsiek & Weller 2008; Williams *et al*. 2009; Flores-Orozco *et al*. 2011). Such a geophysical method is called complex resistivity, complex conductivity, (time- or frequency-domain) induced polarization or low-frequency dielectric spectroscopy in the literature. In frequency-domain induced polarization, an alternating current is injected and retrieved into the ground using two electrodes A and B. Both the resulting magnitude and phase of the voltage between two potential electrodes M and N are measured and used to define impedance, which once corrected for the position of the electrode is used to define an apparent complex resistivity. This method was originally developed for the exploration of ore bodies (Pelton *et al*. 1978; Seigel *et al*. 2007). The sensitivity enhancement of modern equipment has increased the measurement resolution of the phase lag between the current and the voltage (typically 0.1 mrad in the laboratory up to 100 Hz and 0.4 mrad in the field with a 24 bit acquisition card, see discussion in G. Olhoeft, personal communication 2010 and Vaudelet *et al.* 2011a,b). This instrumentation has made possible the use of the induced polarization method in environmental investigations (for which the phase lag is usually very small, <20 mrad), such as the detection of organic and inorganic contaminants (Olhoeft 1985, 1986; Börner *et al.* 1993; Schmutz *et al*. 2010) and the determination of permeability (e.g. Börner *et al*. 1996; Kemna *et al*. 2004; Binley *et al*. 2005; Hördt *et al*. 2007; Revil & Florsch 2010).

Recently, Revil *et al.* (Leroy *et al*. 2008; Leroy & Revil 2009; Revil & Florsch 2010; Schmutz *et al*. 2010) have also provided a complete theoretical framework explaining induced polarization measurements in terms of polarization of the electrical double layer coating on the surface of the grains. They followed previous works done by de Lima & Sharma (1992) and Lesmes & Morgan (2001). However, all these approaches do not include a description of membrane polarization and a unified model including this contribution has still to be done. The approach described in Leroy *et al*. (2008) can be used to provide a physical explanation for the Cole–Cole model, which is broadly used to interpret induced polarization measurements in the laboratory or in the field (Pelton *et al.* 1978; Ghorbani *et al*. 2007; Florsch *et al*. 2010).

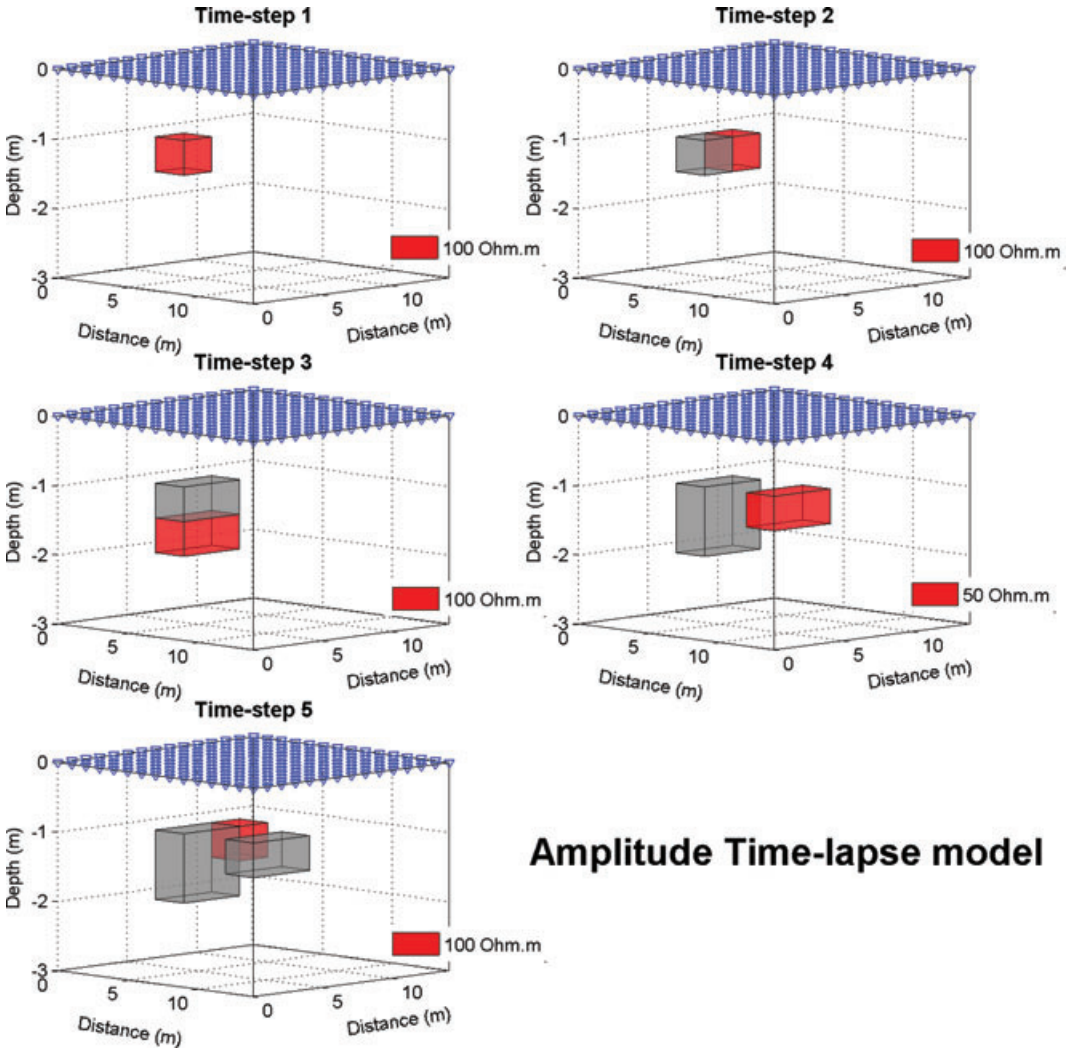


Figure 1. The 4-D induced polarization model used in this work showing the changes in amplitude through time (five time steps). The grey cubes denote the synthetic model used in the previous time step. The red cubes show the change in that time step with respect to the previous time steps. The background model has a constant resistivity amplitude of 10 Ω m.

Downloaded from https://academic.oup.com/gji/article/187/1/237/561878 by guest on 02 March 2021

Several single time step inversion algorithms have been proposed to invert induced polarization data, either involving frequency-domain complex resistivity modelling (Kemna & Binley 1996; Shi *et al*. 1998; Kemna *et al*. 2000) or time-domain chargeability modelling (Routh *et al.* 1998; Loke *et al.* 2006). The introduction of time into the inversion of geophysical data sets can be achieved with the use of time-lapse algorithms. In this case, several strategies are possible. A standard approach is to independently invert the measured data acquired at each monitoring step and to reconstruct time-lapse images (e.g. Daily *et al.* 1992; Ramirez *et al.* 1993; Binley *et al.* 1996). As suggested by several researchers, the independent time-lapse inversion images may be strongly contaminated with inversion artefacts due to the presence of noise in the measurements and independent inversion errors. LaBrecque & Yang (2001) and Kim *et al*. (2009) presented time-lapse algorithms to minimize those artefacts, but as shown by Karaoulis *et al*. (2011), these algorithms may also suppress real changes in the complex resistivity due to the spurious effect associated with the selection of the time regularization parameter in the cost function.

In this work, we describe a new induced polarization time-lapse tomography algorithm. Forward modelling is presented in Section 2. In Section 3, we present a new 4-D algorithm for induced polarization based on an active time constrained (ATC) approach. Our work extends the recent work of Karaoulis *et al.* (2011) for dc resistivity to complex resistivity in the frequency domain. Time-lapse time-domain IP data could be treated the same way. In our approach, the subsurface is defined as a space–time model and the regularization over time is active where it allows variability between different time steps depending on the degree of spatial complex resistivity changes occurring among different monitoring stages (time steps). As a result, the 4-D-ATC algorithm can help in focusing on the 3-D spatio-temporal changes of the complex resistivity. We will present the results for a single-frequency application of the algorithm; however, the extension of the algorithm to multifrequency time-lapse data can be done with the successive application of the algorithm to a set of data taken at distinct frequencies. Along the same lines, the approach of Kemna *et al.* (1999, 2000) for 'static' spectral data provides information about the spectral behaviour of the subsurface complex resistivity. Using spectral-induced polarization data, a relaxation model such as the Cole–Cole model can be fitted for each cell and the evolution of the Cole–Cole parameters can be followed over time.

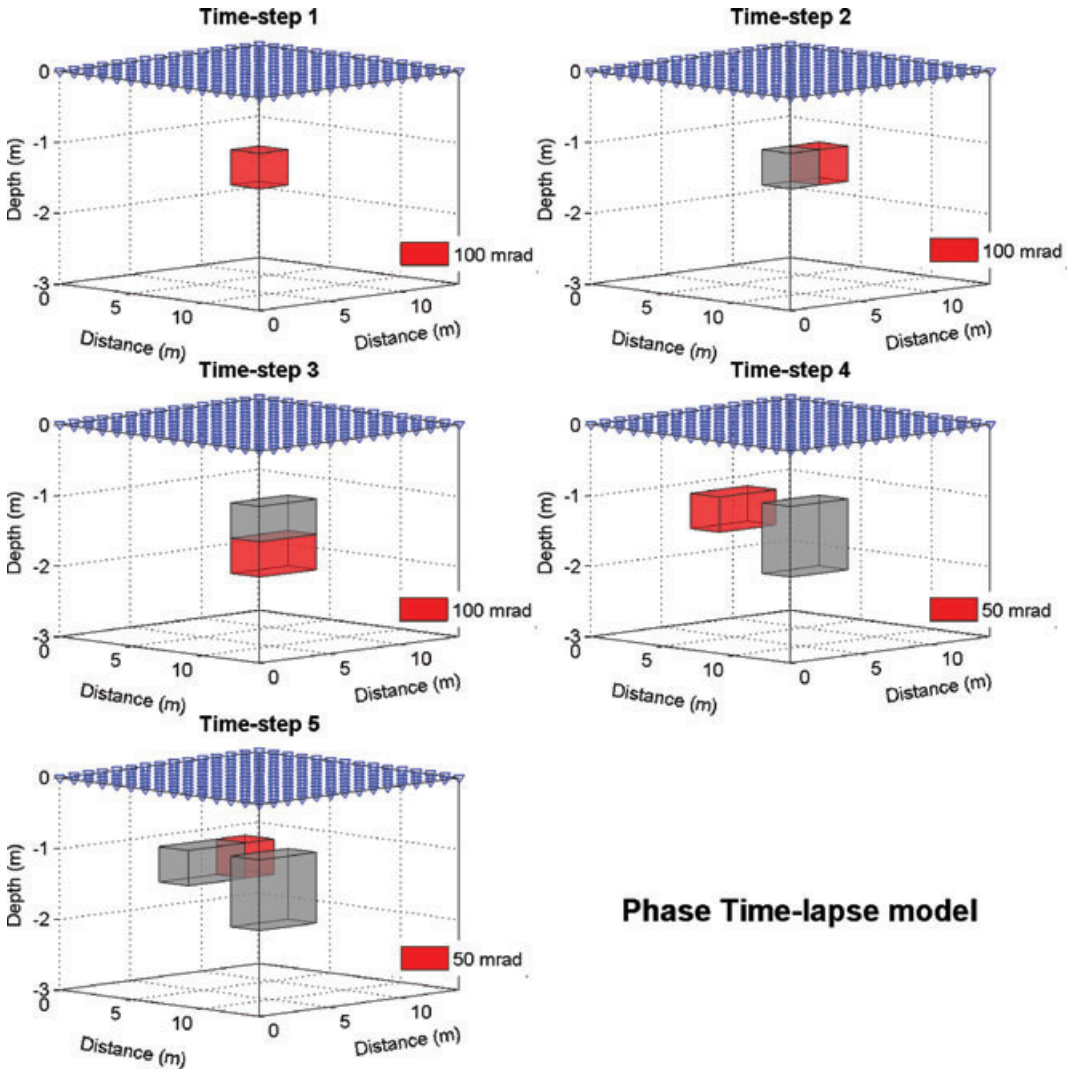


Figure 2. Same as Fig. 1 for the phase lag. The background model has a phase of –5 mrad.

Downloaded from https://academic.oup.com/gji/article/187/1/237/561873 by guest on 02 March 2021

2 FORWARD MODELLING

In the frequency domain, we denote $\omega = 2\pi f$ the angular frequency, f the frequency (in Hertz) and $i = (-1)^{1/2}$ the imaginary unit. The magnitude of the conductivity $|\sigma|$ and the phase lag $\varphi \in [-\pi, \pi]$ between the excitation current and the resulting electrical field are related to the real (in-phase) and imaginary (out-of-phase or quadrature) components of the complex conductivity σ^*, σ' and σ', respectively, (expressed in S m^{-1}), by

$$\sigma^* = |\sigma| \exp(\mathrm{i}\varphi) = \sigma' + \mathrm{i}\sigma''. \quad (1)$$

In this equation, $|\sigma| = (\sigma'^2 + \sigma''^2)^{1/2}$ and $\varphi = \mathrm{atan}(\sigma''/\sigma')$ represents frequency-dependent amplitude and phase of conductivity, respectively. Induced polarization is usually displayed as a resistivity (or conductivity) magnitude $|\rho| = 1/|\sigma|$ (in ohm m) and a phase lag φ (in rad) or alternatively as an in-phase conductivity σ' and a quadrature conductivity σ'', respectively. The complex conductivity is related to the complex resistivity ρ^* by,

$$\sigma^* = \frac{1}{\rho^*}, \quad (2)$$

where $\rho^* \neq 0$. In practice, an alternating current is used to perform spectral or frequency-domain IP measurements. For a given current, both the amplitude of the voltage and the phase lag between the current and the voltage are measured. The impedance can be multiplied by the same geometrical factor as used for dc-resistivity (e.g. Kemna 2000) to provide the amplitude of the apparent electrical conductivity at each frequency. The phase lag is however independent of the geometric factor.

In the forward modelling of the induced polarization problem, the electric potential can be expressed as a complex number (e.g. Kemna 2000)

$$V(\omega) = V'(\omega) + \mathrm{i}V''(\omega). \quad (3)$$

The amplitude of the voltage and the phase lag are given by,

$$|V(\omega)| = \sqrt{[V'(\omega)]^2 + [V''(\omega)]^2}, \quad (4)$$

$$\varphi(\omega) = \mathrm{atan}\left[\frac{V''(\omega)}{V'(\omega)}\right]. \quad (5)$$

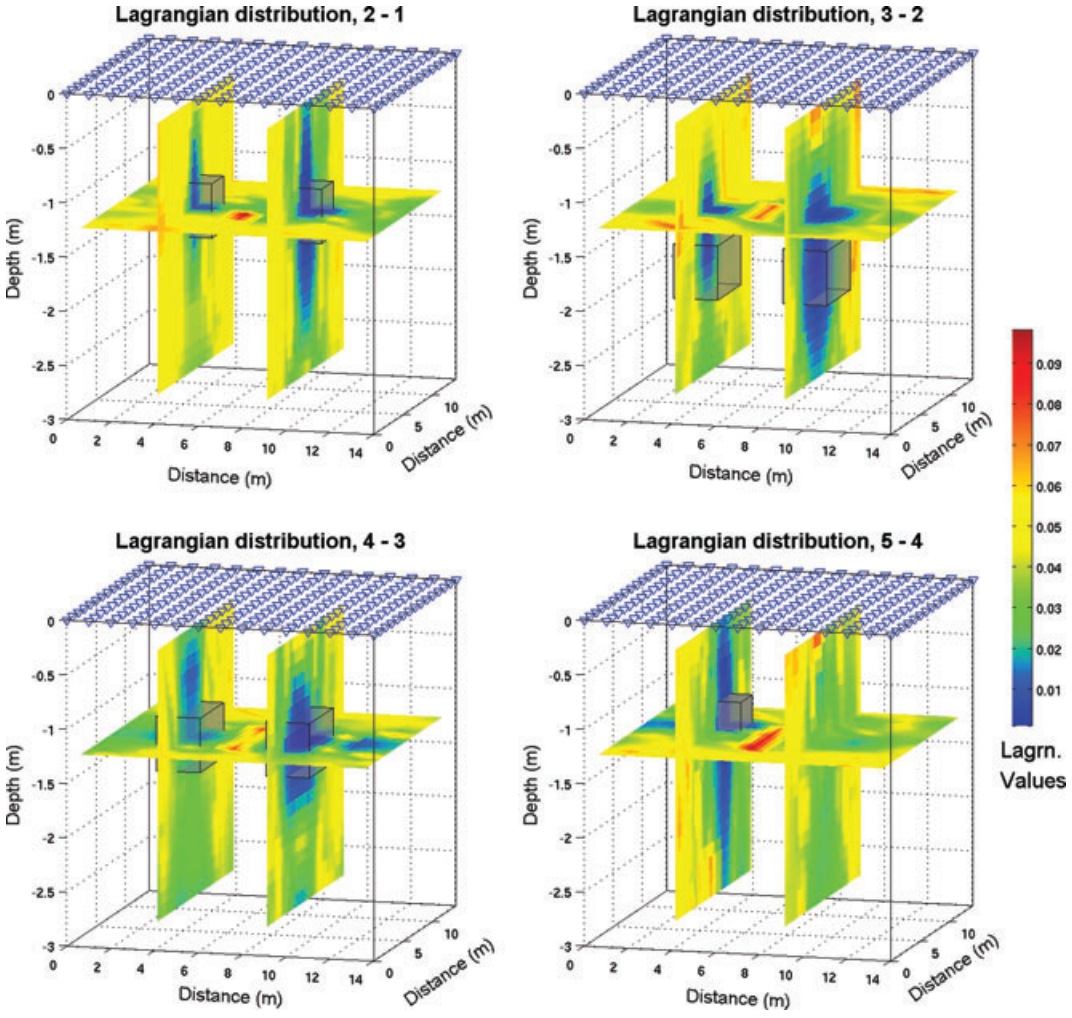


Figure 3. The distribution of Lagrange parameters based on the independent inversion as a prior information used in the ATC approach. The cold colours indicate areas with significant changes. These areas are characterized by low values of the Lagrange parameters. The hot colours indicate areas with no changes, that is, areas characterized by high values of the (Lagrange) regularization parameters. The grey cubes show the position of the true changes in the synthetic model.

Downloaded from https://academic.oup.com/gji/article/187/1/237/561878 by guest on 02 March 2021

In the following, we will neglect electromagnetic coupling effects, which is a good approximation at low frequencies (<100 Hz, see e.g. Kemna 2000).

The relation between the complex conductivity and the complex potential is given by (Weller *et al.* 1996)

$$\nabla \cdot [\sigma(x, \omega)\nabla V(x, \omega)] = -I(\omega)\delta(\boldsymbol{x} - \boldsymbol{x}_S), \tag{6}$$

where $\boldsymbol{x}$ is the position vector and $I(\omega)$ is the injected current (in Ampere) at frequency ω represented as a point source at position $\boldsymbol{x}_s$, where δ represents a delta function.

Eq. (6) is a Poisson equation, which can be solved for given boundary conditions using the finite-element method (Kemna 2000). The basic concept of the finite-element method is to subdivide the investigated domain into n_e elements in which the unknown potential $V(\omega)$ is approximated by means of discrete values at the nodes of the elements. Assuming homogeneous and isotropic elements, the solution of the Poisson equation can be obtained in discrete form by solving a system of linear equations

$$\boldsymbol{K}(\omega)\boldsymbol{V} = \boldsymbol{F}, \tag{7}$$

where the kernel matrix $\boldsymbol{K}(\omega)$ ($n_e \times n_e$) consists of individual element matrices of each element; these are the same as for the real-valued (dc) problem because all terms are related only to the nodal coordinates, and the multiplication with the complex resistivity transforms the system into a relationship involving complex numbers. The explicit form of this matrix for the hexahedron elements used below is given in Tsourlos & Ogilvy (1999). The vector $\boldsymbol{V}$ contains the nodal values of the complex potential and the vector $\boldsymbol{F}$ (n elements) contains the current sources.

In this work, we used mixed boundary conditions, which can be implemented in the complex case analogous to the dc case (Kemna 2000). A Neumann boundary condition is imposed at the ground surface (there is no current flow normal to this boundary) and a finite value is set on the half-space boundaries, which is determined by the asymptotic behaviour of the potential for a homogeneous half-space (Dey & Morrison 1979).

3 TIME-LAPSE INVERSION

We present now the 4-D algorithm used to perform the time-lapse inversion. Kim *et al*. (2009) defines the subsurface as a space–time model, which encompasses all space models during the entire monitoring period. The entire monitoring data are defined as a data vector in the space–time domain as well. The space–time model is assumed to change continuously along the time-axis, which allows the change of the subsurface material property distribution

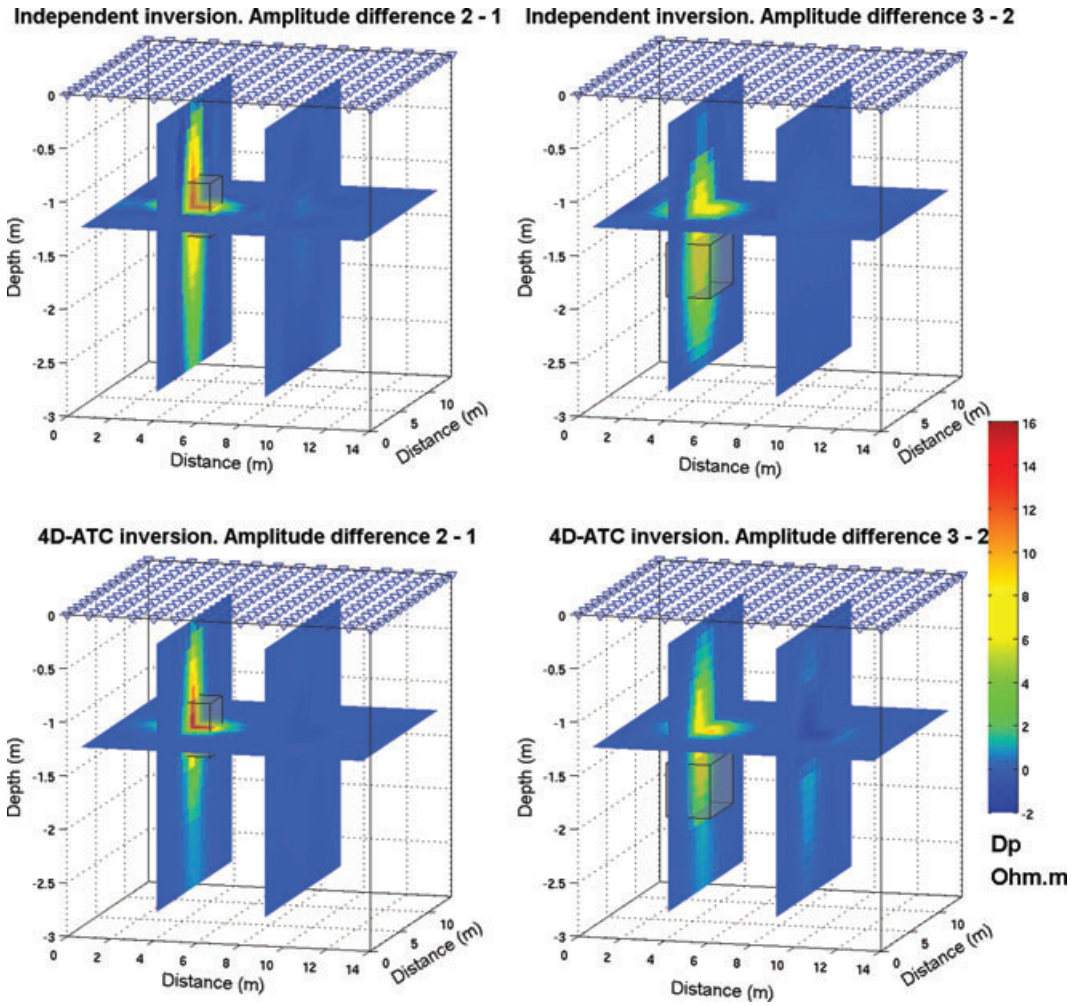


Figure 4. Difference images for the synthetic model of resistivity presented in Figs 1 and 2. The 4-D-ATC (lower row) and independent inversion (upper row) difference amplitude images are shown for time steps 2–1 (left side) and 3–2 (right side), respectively. The grey cube shows the position of the true change according to the synthetic model.

Downloaded from https://academic.oup.com/gji/article/187/1/237/561873 by guest on 02 March 2021

during the measurement of the geophysical datum. Assuming a model that is sparsely sampled at pre-selected times, the 4-D subsurface model $\tilde{\boldsymbol{X}}$ for all the time steps of the monitoring data is expressed as $\tilde{\boldsymbol{X}} = [\boldsymbol{X}_1, \cdots, \boldsymbol{X}_t]^T$, where $\boldsymbol{X}_i$ is the reference space model, a matrix of complex elements describing the complex resistivity distribution, for the ith time step and t denotes the number of monitoring times. The data misfit vector is defined in the space–time domain by

$$\mathrm{e}^{k+1} = \hat{\boldsymbol{D}} - G(\tilde{\boldsymbol{X}}^{k+1}) = \hat{\boldsymbol{D}} - G(\tilde{\boldsymbol{X}}^{k} + \mathrm{d}\tilde{\boldsymbol{X}}), \quad k = 1, 2, \ldots. \tag{8}$$

In Eq. (8), $\hat{\boldsymbol{D}}$ denotes the data vector defined in the 4-D coordinate system by $\hat{\boldsymbol{D}} = [\boldsymbol{d}_1, \cdots, \boldsymbol{d}_t]^T$, where $\boldsymbol{d}_i$ is the data from time step i expressed as a complex number describing the alternating potential, $\boldsymbol{G}(\tilde{\boldsymbol{X}}^k)$ denotes the forward modelling response and $\mathrm{d}\tilde{\boldsymbol{X}} = [\mathrm{d}\boldsymbol{X}_1, \ldots, \mathrm{d}\boldsymbol{X}_t]^T$ is the model perturbation vector, that is, $\mathrm{d}\tilde{\boldsymbol{X}} = \tilde{\boldsymbol{X}}^{k+1} - \tilde{\boldsymbol{X}}^k$, and the superscript k denotes the iteration number.

Because both the data and the model are defined using space–time coordinates, the 4-D-ATC algorithm is able to adopt two regularizations, in both the time and space domains, to stabilize the inversion. Consequently, we are looking to minimize the following objective function T (Zhang *et al*. 2005; Kim *et al*. 2009),

$$T = \left\|\mathrm{e}^T \mathrm{e}\right\|^2 + \lambda\Psi + \alpha\,\Xi, \tag{9}$$

where Ψ and Ξ are the two regularization functions/penalty terms. The function Ψ is used for smoothness regularization in space and the function Γ is used for smoothness regularization in time. The two parameters, λ and α, are the regularization parameters (also called the Lagrange parameters in literature). Regarding the smoothness in the space domain, a second-order differential operator is applied to the model perturbation vector $d\hat{\boldsymbol{X}}$. In the time domain, Kim *et al*. (2009) applied a first-order differential operator to the model vector $\hat{\boldsymbol{X}}$. This assumption is consistent with the idea that the change over time of the material properties is smaller compared to their changes in space. Therefore, in our approach, the subsurface structure remains nearly the same throughout the entire monitoring period. Following these principles, the two regularization functions in the cost function, Eq. (9), Ψ and Ξ, are defined as

$$\Psi = (\partial^2 \mathrm{d}\hat{\boldsymbol{X}})^T (\partial^2 \mathrm{d}\hat{\boldsymbol{X}}), \tag{10}$$

$$\Xi = \sum_{i=1}^{t-1} \left\|\boldsymbol{X}_{i+1}^{k+1} - \boldsymbol{X}_i^k\right\|^2 = \left\{\boldsymbol{M}(\boldsymbol{X}^k + \mathrm{d}\boldsymbol{X})\right\}^T \boldsymbol{M}(\boldsymbol{X}^k + \mathrm{d}\boldsymbol{X}), \tag{11}$$

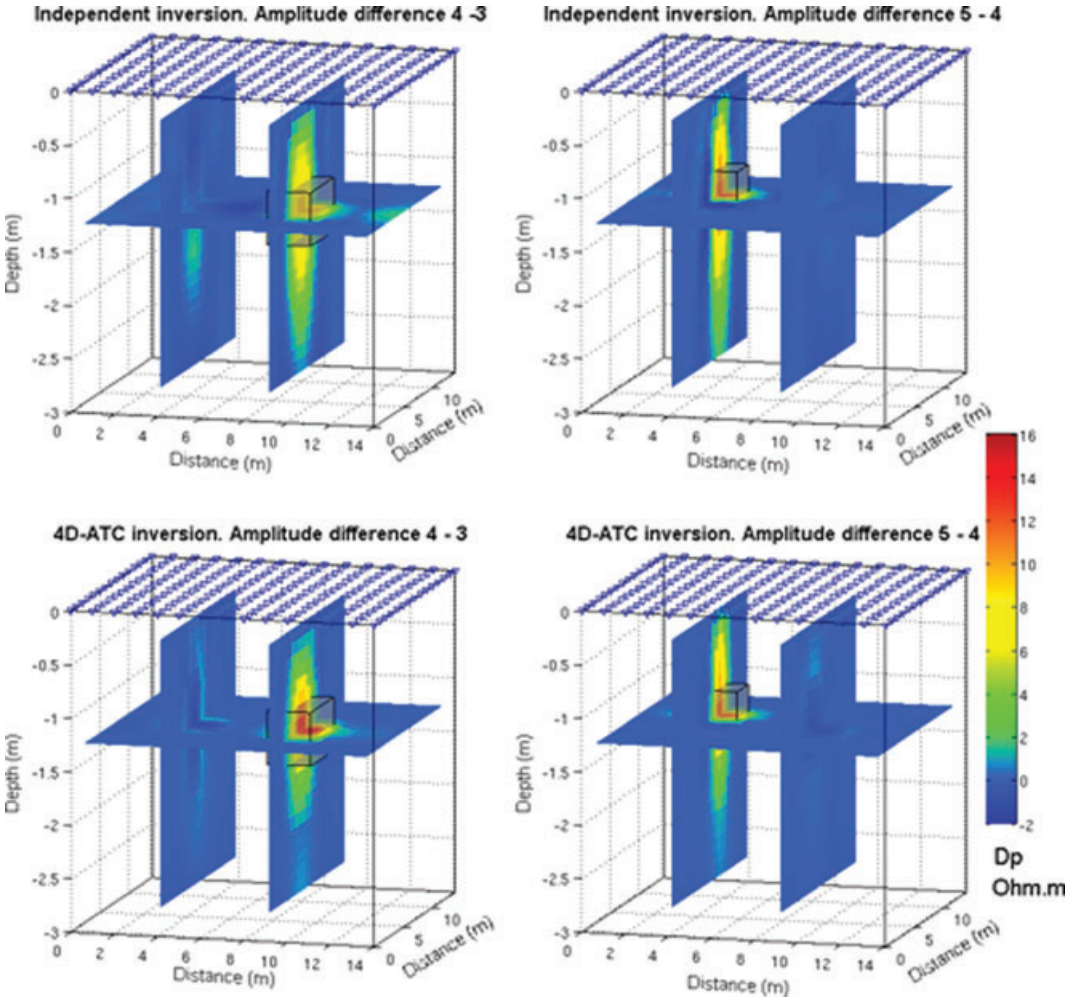


Figure 5. Difference images for the synthetic model of resistivity presented in Figs 1 and 2. The 4-D-ATC (lower row) and independent inversion (upper row) difference amplitude images are shown for time steps 4–3 (left side) and 5–4 (right side), respectively. The grey cube shows the localization of the true change from the synthetic model.

Downloaded from https://academic.oup.com/gji/article/187/1/237/561878 by guest on 02 March 2021

respectively, where $\boldsymbol{M}$ ($nt \times nt$ elements) is a square matrix. Only the diagonal and one subdiagonal element of this matrix have non-zero values, 1 or –1, to add constrains for the same parameters in adjacent time steps.

In our approach, the space-domain Lagrangian is expressed as a diagonal matrix $\hat{\boldsymbol{\Lambda}}(nt \times nt$ elements) because the active constraint balancing (ACB) is adopted for the space-domain regularization (Yi *et al*. 2003). The time-domain Lagrangian is expressed as a diagonal matrix $\boldsymbol{A}$ (Karaoulis *et al*. 2011), which offers flexibility to describe relatively rapid time changing phenomena. In particular, by allowing the time-Lagrangian multiplier to change in both space and time domain, the matrix $\boldsymbol{A}$ is a diagonal matrix with dimensions ($nt \times nt$ elements), where n is the number of the parameters of a space model at each reference time. Therefore, $\boldsymbol{A}$ can take discrete values for every space parameter of every time step making the time-related regularization active. Obviously, if $\boldsymbol{A}$ is a zero matrix, then the 4-D-ATC equation is transformed into independent inversions. From eqs (9) to (11), the final objective function T to be minimized is, therefore, given by

$$T = \left\|\mathrm{e}^T\mathrm{e}\right\|^2 + (\partial^2 \mathrm{d}\hat{\boldsymbol{X}})^T \hat{\boldsymbol{\Lambda}} (\partial^2 \mathrm{d}\hat{\boldsymbol{X}}) + \left\{\boldsymbol{M}(\hat{\boldsymbol{X}}^k + \mathrm{d}\hat{\boldsymbol{X}})\right\}^T \boldsymbol{A}\boldsymbol{M}(\hat{\boldsymbol{X}}^k + \mathrm{d}\hat{\boldsymbol{X}}), \quad (12)$$

where the matrix $\hat{\boldsymbol{\Lambda}}$ ($nt \times nt$ elements) denotes a diagonal matrix for the ACB in the space domain (Yi *et al.* 2003), $\hat{\boldsymbol{\Lambda}} = \mathrm{diag}[\boldsymbol{\Lambda}_1, \boldsymbol{\Lambda}_2, \ldots, \boldsymbol{\Lambda}_t]$, where $\boldsymbol{\Lambda}_i$ is the ACB matrix for the model at time i.

Minimizing the objective function given in eq. (12) with respect to the model perturbation vector yields the following normal equations (Kim *et al.* 2009):

$$\tilde{\boldsymbol{X}}^{k+1} = \tilde{\boldsymbol{X}}^k + \mathrm{d}\tilde{\boldsymbol{X}}, \quad (13)$$

$$\mathrm{d}\tilde{\boldsymbol{X}} = \left(\hat{\boldsymbol{j}}^T\hat{\boldsymbol{j}} + \hat{\boldsymbol{C}}^T\hat{\boldsymbol{\Lambda}}\hat{\boldsymbol{C}} + \boldsymbol{M}^T\boldsymbol{A}\boldsymbol{M}\right)^{-1} \times \left\{\hat{\boldsymbol{j}}^T\left[G(\tilde{\boldsymbol{X}}^k) - \hat{\boldsymbol{D}}\right] - \boldsymbol{M}^T\boldsymbol{A}\boldsymbol{M}\tilde{\boldsymbol{X}}^k\right\}. \quad (14)$$

In eq. (14), $\hat{\boldsymbol{j}}$ ($n_m t \times nt$ elements) denotes the sensitivity matrix (or Jacobian) and n_m the number of measurements from each time step. We consider that during the record of a single time step data set $\boldsymbol{d}_i$, the changes of the conductivity of the subsurface can be neglected, $\hat{\boldsymbol{j}}$ can be expressed as a block diagonal matrix (Kim *et al.* 2009)

$$\hat{\boldsymbol{j}} = \mathrm{diag}\left[\boldsymbol{J}_1, \boldsymbol{J}_2, \ldots, \boldsymbol{J}_t\right] = \begin{bmatrix} \boldsymbol{J}_1 & 0 & 0 & 0 \\ 0 & \boldsymbol{J}_2 & 0 & 0 \\ & & \ddots & \\ 0 & 0 & 0 & \boldsymbol{J}_t \end{bmatrix}, \quad (15)$$

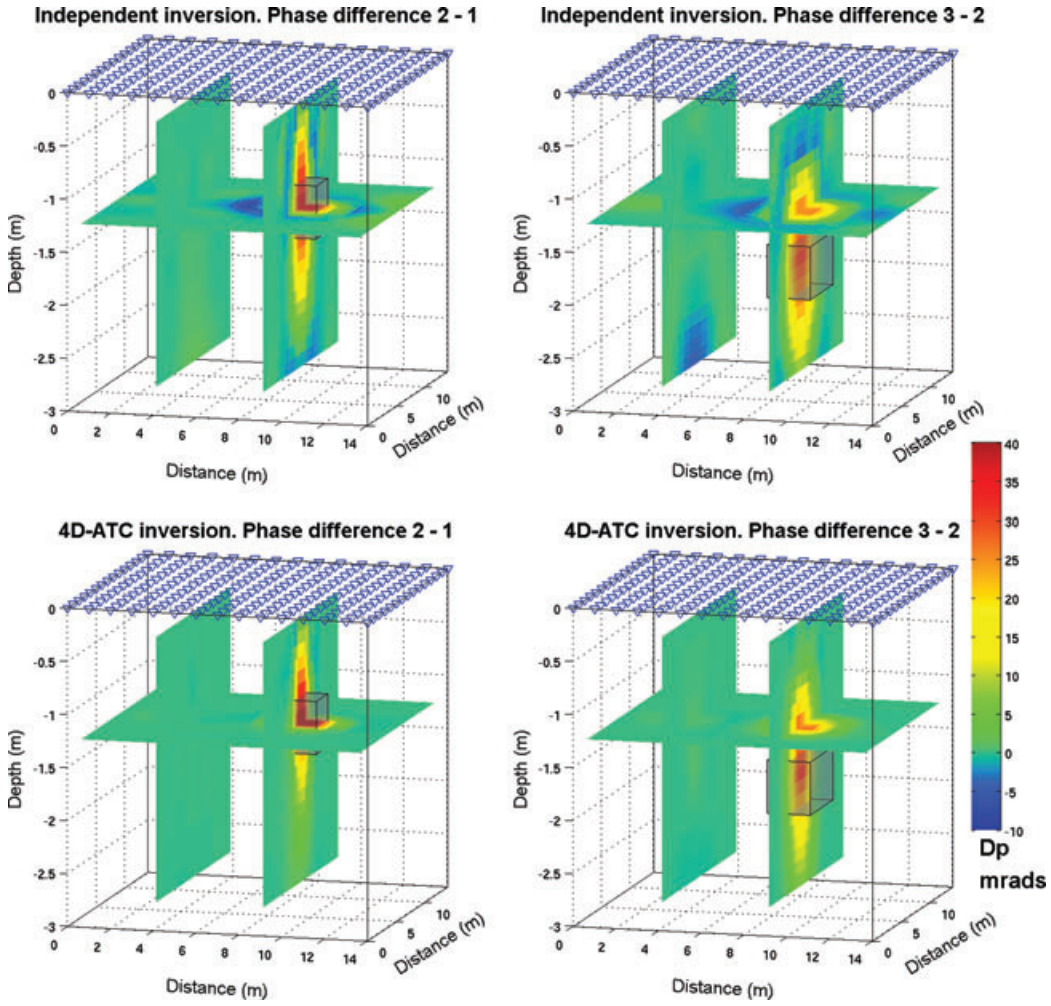


Figure 6. Same as Fig. 4 for the phase.

Downloaded from https://academic.oup.com/gji/article/187/1/237/561873 by guest on 02 March 2021

for a number t of distinct times. The matrix $\boldsymbol{J}_i$ denotes the sensitivity matrix at time i. For the definition and computation of the complex-valued sensitivity for the complex conductivity problem using the adjoint technique, we refer the readers to Kemna (2000). When the subsurface conductivity changes during each data acquisition, the assembled sensitivity matrix is no longer a block diagonal matrix as explained in Kim *et al.* (2009). The matrix $\hat{\boldsymbol{C}}$ is the differential operator in the space domain. It is given by $\hat{\boldsymbol{C}} = \text{diag}[\boldsymbol{C}_1, \boldsymbol{C}_2, \cdots, \boldsymbol{C}_t]$, where $\boldsymbol{C}_i$ is the differential operator for the space-model of time i (Oldenburg *et al.* 1993).

The active time Lagrangian, expressed with the matrix $\boldsymbol{A}$, controls the time-related changes. Effectively, such a scheme should vary the time normalization between the parameters of different time steps proportionally to the spatial resistivity changes occurring amongst different monitoring locations. The determination of the time regularization parameter may depend on the spatio-temporal characteristics of the process, which is controlling the changes in complex resistivity. Ideally, matrix entries associated with areas of significant property changes must be assigned low time regularization values and vice versa. Two methods are proposed to assign the appropriate values to the time regularization parameter: one based on a fast pre-estimation of the first independent inversion iteration and one, more accurate, after a full inversion (Karaoulis *et al.* 2011). In this work, we used the accurate calculation of the time Lagrange matrix.

The creation of the matrix $\boldsymbol{A}$ is similar to the dc (real values) problem with one exception. In the induced polarization case, two models must be considered, one for time-lapse changes in the amplitude and one for the time-lapse changes of the phase. Note that the resistivity and the phase can change over time independently from each other (see Vaudelet *et al.* 2011a,b, for laboratory examples). The values of the Lagrangian parameters should be low for areas that show time-lapse changes in amplitude and/or phase.

To perform this task, we follow the following steps: (1) we generate a time-related distribution of values for the Lagrangian parameter as a function of the difference in amplitude between two sequential time steps, (2) we generate a time-related distribution of values for the Lagrangian parameter from the difference in phase between two sequential time steps and (3) we combined these two time-related Lagrangian value distributions in one scheme (e.g. for a specific subregion use as final value, the minimum value between amplitude and phase distributions). Trial-and-error testing showed that for our numerical examples the two time-related Lagrangian values must be between 0.01 and 0.1.

4 THREE-DIMENSIONAL SYNTHETIC TEST

The 4-D-ATC algorithm is going to be tested with synthetic data and compared to the prediction of using independent inversion

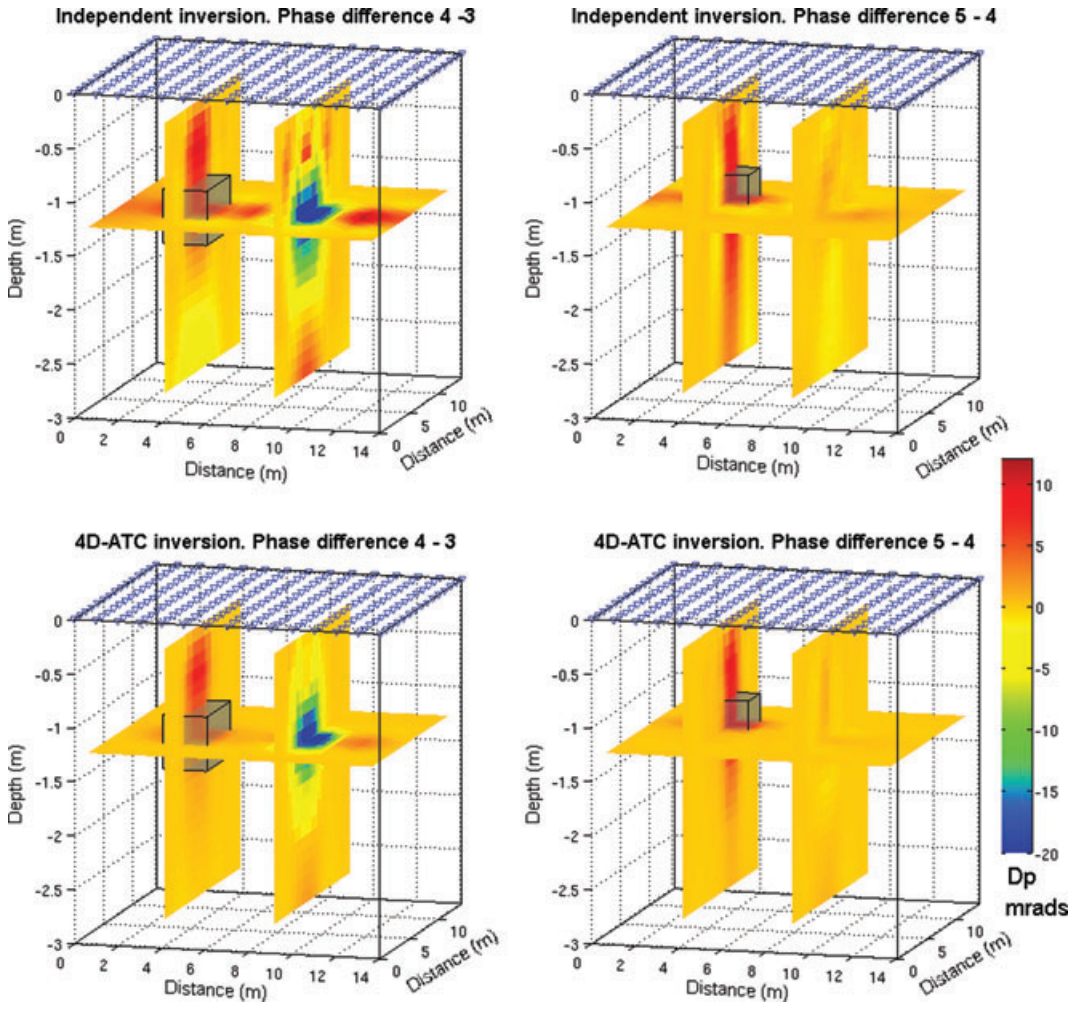


Figure 7. Same as Fig. 5 for the phase.

Downloaded from https://academic.oup.com/gji/article/187/1/237/561878 by guest on 02 March 2021

tomographies (performed independently at each time step). In the case of field data, it is expected that the artefacts associated with the presence of noise in the data is significant and independent inversion must, therefore, be avoided. For the comparison between the two approaches to be objective, all algorithms were based on the same 3-D finite element forward modelling and inversion platform, the principles of this platform having already been discussed in Section 2. Note that the same homogeneous half-space was used as the starting model for all the tested techniques and that all the synthetic data are considered as measured simultaneously for each time step. In this paper, the phase and amplitude are shown (it is implicit that the phases have negative values). The data misfit was smaller than 5 per cent for the two examples discussed later.

4.1 Synthetic model and time-Lagrangian distribution

Modelled data obtained for five different time steps representing a hypothetical time-lapse induced polarization change are depicted in Figs 1 and 2. A total of 225 surface electrodes were used to obtain surface dipole–dipole data (interelectrode spacing $a = 1$ with maximum intradipole spacing d$n = 7$). The pseudosection comprises a total of 945 measurements for each time step. In this specific example, the synthetic data are taken noise-free. The background model had amplitude of 10 Ω m for the amplitude of the resistivity and 5 mrad for the amplitude of the phase.

Figs 1 and 2 show the modelled evolution of both the amplitude of the resistivity and the amplitude of the phase. The grey cubes show the changes (in both amplitude and phase) that remain stable through time. Red cubes reveal the modelled changes in both the amplitude of the resistivity and that of the phase between two sequential time steps. For instance, the red cube shown in time step 1 in amplitude, remains stable from time step 2 on (so it is denoted as grey in all later time steps), where a new red cube is introduced, which shows the modelled change between those two time steps.

As discussed in Section 4, the 4-D-ATC technique requires *a priori* information on the expected time related changes, so the matrix $\boldsymbol{A}$ could be formulated. Fig. 3 shows the distribution of the time Lagrangian values used as *a priori* information. The $\boldsymbol{A}$ matrix must consider time related changes in both amplitude and phase, to adjust appropriate weight. Cold colours, that is, low values on the time-related Lagrangian, indicate areas with expected changes in both amplitude and phase and hot colours (large time-related Lagrangian values) indicate areas with no time changes. Therefore, Fig. 3 shows, with grey cubes, the actual changes in both amplitude and phase in the same figure. The relation between low time-related Lagrangian values with the actual changes is quite good, even considering the fact that the estimation seems to be spread. Note that the $\boldsymbol{A}$ matrix is just a pre-estimation of where the expected change is located between two time steps. The $\boldsymbol{A}$ matrix was calculated using the full independent inversion of each data set. In Figs 4 and 5, the first series of images (upper part) shows the difference in amplitude between two sequential time steps; in Figs 6 and 7, the first series of images (upper part) denotes the difference in the phase. A combination of the amplitude and phase time-related changes is then used to create the matrix $\boldsymbol{A}$ (Fig. 3).

4.2 Inversion results

The second rows of Figs 4–7 show the difference inversion images produced using the 4-D-ATC technique. Grey cubes represent the modelled time changes. Generally, when compared with the independent inversion inversion artefacts are reduced and at the same time, the actual change is shown in a clearer way. The areas of the actual changes, when using the 4-D-ATC technique, are represented in a more compact form and as discussed in Section 4, the partial unsuccessful choice of pre-estimation when creating the matrix $\boldsymbol{A}$ does not affect the final difference images. Custom $\boldsymbol{A}$ matrices, based on more geological information than resistivity data, can significantly reduce artefacts and help focus on the real changes. Both techniques create an artefact of reduced phases between time steps 3 and 4, which indicate the difficulties obtaining information when time-related changes are robust. In those cases, higher orders of time-specific regularization should be used.

Fig. 8 shows the percentage rms fit between the original (true) model and the final inversion result for every time step. The 4-D-ATC exhibits the smaller percentage model rms misfit (real number), in all cases, except at time step #1. The percentage error misfit regarding the magnitude of the phase is significantly larger than for the amplitude of the resistivity. This is due to the small expected values of the phase when compared to the amplitude (e.g. Kemna 2000). This problem can be partially addressed using inversion techniques like final phase improvement (Kemna 2000) for which additional iterations are used only for the phase. Figs 9 and 10 show the final inversion models using the 4-D-ATC technique. The grey cubes denote the modelled change. We observe that the inversion models are in good agreement with the true models.

5 ATC-BASED TOMOGRAPHY OF A SALT TRACER TEST

To investigate the effect of heterogeneity in the Earth's subsurface on the time-lapse ATC technique, a 2-D stochastic model was used to simulate a salt tracer test injection. This stochastic model was

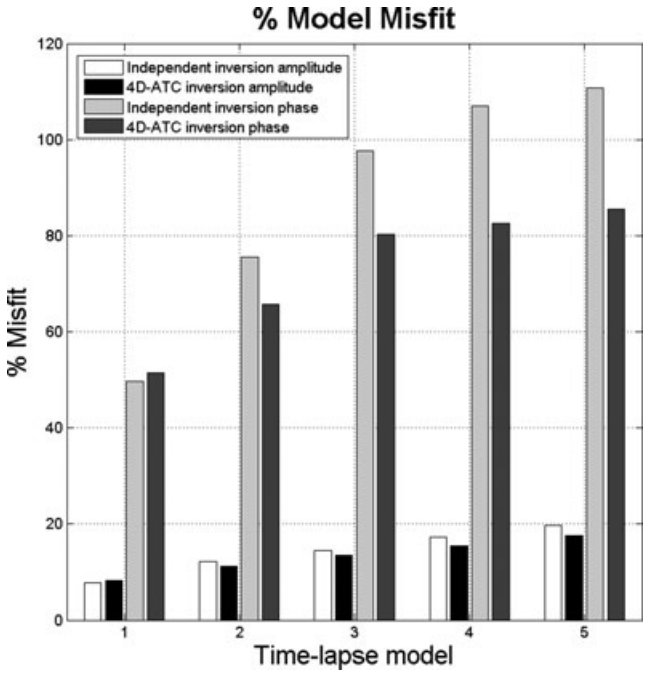


Figure 8. Percent model misfit for independent and 4-D-ATC inversion (amplitude and phase). Note the lower rms error associated in general with the ATC-based approach, in both the amplitude and phase. The lower per cent model misfit error between the inversion methods is an indication that the 4-D-ATC approach produces a more realistic model.

Downloaded from https://academic.oup.com/gji/article/187/1/237/561873 by guest on 02 March 2021

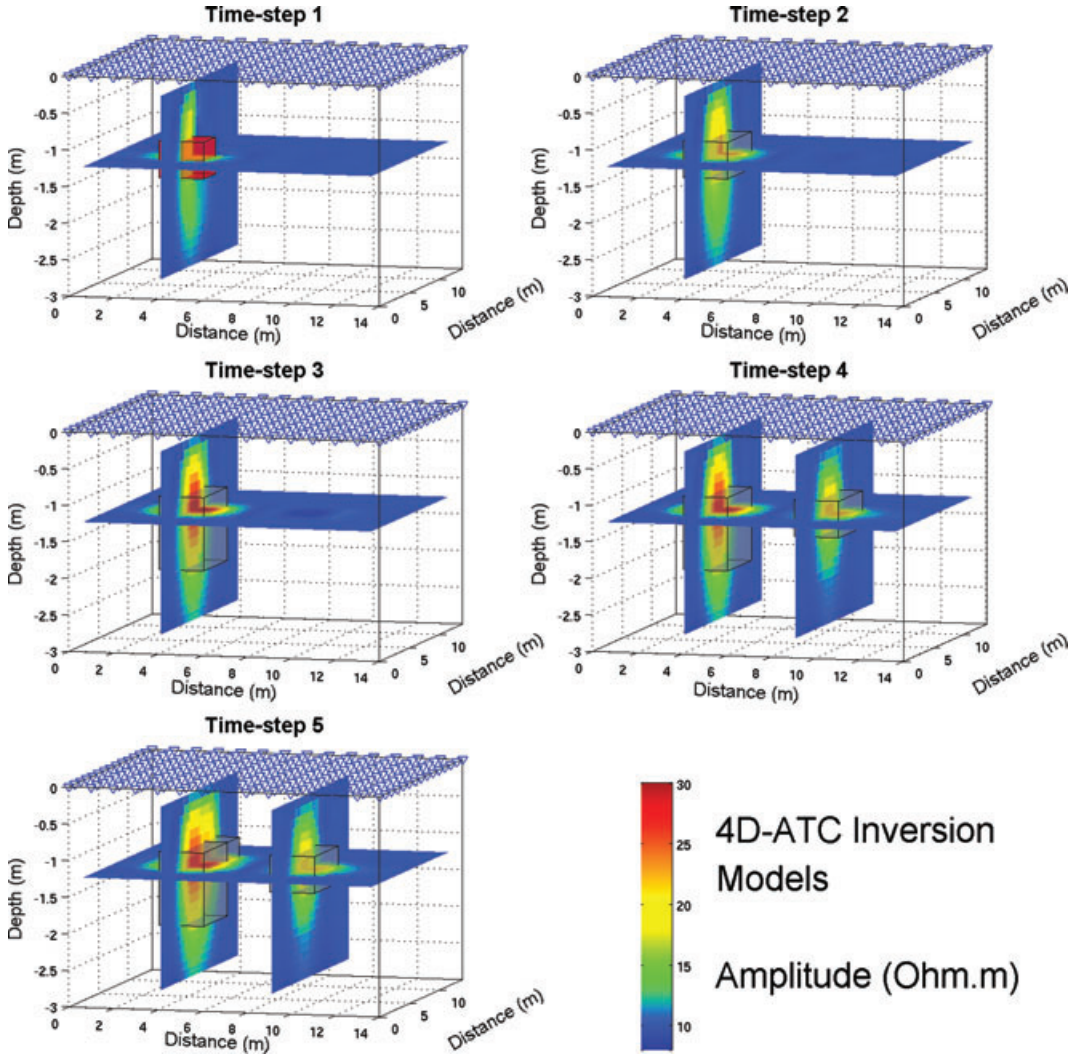


Figure 9. The 4-D-ATC inversion model showing the amplitude of each model time step. The grey cube shows the true change in amplitude of the resistivity.

used to generate a realistic synthetic data set of the Earth subsurface to test the inversion algorithm.

5.1 Stochastically generated heterogeneous aquifer

A heterogeneous aquifer with a stochastic distribution of the transport parameters was generated using the Stanford Geostatistical Modeling Software package (SGeMS, see Remy *et al*. 2009). Several stochastic models were realized with the sequential Gaussian simulation algorithm (SGSIM, see Remy *et al*. 2009, p. 135) on a 2-D, 500 × 100 Cartesian grid, $\mathbf{h}(x, z)$, using an asymmetric semi-variogram for simple kriging defined as,

$$\gamma(\boldsymbol{h}) = c_0\gamma^0 + c_1\gamma^1(\boldsymbol{h}), \tag{16}$$

where $c_0\gamma^0$ is a nugget effect with constant $c_0 = 10^{-3}$ and an anisotropic spherical Gaussian semi-variogram $c_1\gamma^1(\boldsymbol{h})$ with major, medium and minor ranges of 75, 50 and 25, respectively, and a null (longitudinal) azimuth, dip and rake. A single realization $\boldsymbol{m}$ was chosen to define the heterogeneous parametric distribution for the finite element simulations of the salt tracer test described below.

This geostatistical model was normalized and scaled as both linear and logarithmic distributions, such that $\boldsymbol{m}$ belongs to the interval (0, 1) for linearly distributed parameters and the logarithm (in base 10) of m belongs to the interval $(0, N)$ for log-distributed parameters where N is the number of decades spanned by a given parameter. These models are shown in Fig. 11. Parameters were mapped into the geostatistical model space by scaling $\boldsymbol{m}$ by a range of parameter values. For linearly distributed parameters (like the porosity ϕ), we use the following function,

$$\boldsymbol{m}_i = \boldsymbol{m}^i_{\min} + n\boldsymbol{m}, \tag{17}$$

where $\boldsymbol{m}_i$ is the mapped parameter distribution, $\boldsymbol{m}^i_{\min}$ is the lower limit of a given parameter i and n is scalar defined as $n = \boldsymbol{m}^i_{\max} - \boldsymbol{m}^i_{\min}$. For log-distributed parameters, we use

$$\boldsymbol{m}_i = \boldsymbol{m}^i_{\min} m. \tag{18}$$

For example, the permeability $\boldsymbol{k}$ is estimated to comprise values ranging from 10^{-12} m^2 to 10^{-17} m^2; hence, permeability is mapped to the model space with eq. (18) using $\boldsymbol{m}^i_{\min} = 10^{-17}$ m^2 and $N = 5$.

The constitutive equations are Darcy's law for the Darcy velocity $\boldsymbol{u}$ (in m s^{-1}), a generalized constitutive equation for the flux density of the salt $\mathbf{j}_d$ (in kg m^{-2} s^{-1}) and including an advection term in addition to the diffusion/dispersion term (Fick's law) and Ohm's law for the current density $\mathbf{j}$ (in A m^{-2}),

$$\mathbf{u} = \phi\mathbf{v} = -\frac{1}{\eta_f}k\nabla p, \tag{19}$$

Downloaded from https://academic.oup.com/gji/article/187/1/237/561878 by guest on 02 March 2021

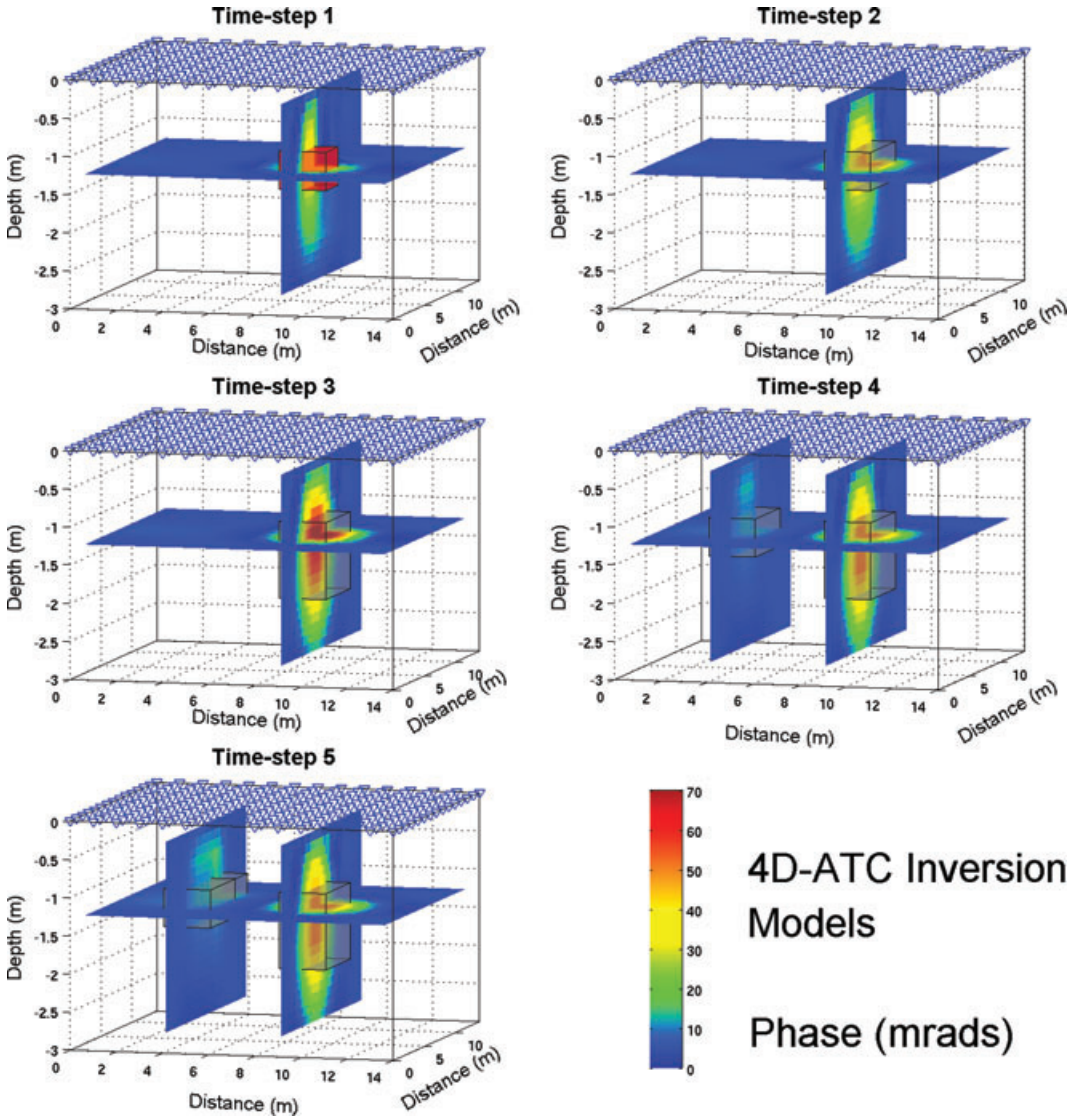


Figure 10. The 4-D-ATC inversion model of the phase at different time steps. The grey cubes show the localization of true changes in the phase.

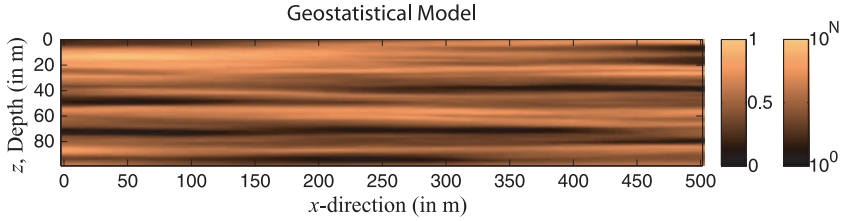


Figure 11. Geostatistical 2-D model used for the simulation of the salt tracer test injection. This synthetic aquifer is generated with a horizontal correlation length that is stronger than the vertical correlation length. The water flows from the left to the right. Each cell is characterized by an isotropic frequency-dependent resistivity. The injection point for the salt injection is located at $x = 5$ m and $z = 5$ m. Only a subset of this domain is used for the time-lapse induced polarization test. The flow is from left to right.

$$\mathbf{j}_d = -\rho_f \phi \mathbf{D} \cdot \nabla C_m + \rho_f \phi \mathbf{v} C_m, \tag{20}$$

where $\mathbf{v}$ is the mean velocity of the pore water (m s^{-1}), $\boldsymbol{D}$ (in m^{2}s^{-1}) is the hydrodynamic dispersion tensor, p is the pore fluid pressure (in Pa), C_m is the solute mass fraction (dimensionless), η_f is the dynamic viscosity of the fluid (in Pa s) and ρ_f is the mass density of the pore water (in kg m^{-3}). In addition to the constitutive equations, we have to consider two continuity equations for the mass of the pore water and for the mass of the salt,

$$\nabla \cdot (\rho_f \mathbf{u}) = -\frac{\partial(\rho_f \phi)}{\partial t} + \rho_f Q_s, \tag{21}$$

$$\nabla \cdot \mathbf{j}_d = -\frac{\partial(\rho_f \phi C_m)}{\partial t} + \rho_f Q_s C_m^0, \tag{22}$$

where C_m^0 is the solute mass fraction of the salt in the source term and Q_s is a volumetric hydraulic source term for the

Downloaded from https://academic.oup.com/gji/article/187/1/237/561873 by guest on 02 March 2021

Table 1. Stochastic parameters used in the geostatistical model used for the simulation of the salt tracer test.

Parameter	$m^i_{\min}$	$m^i_{\max}$	n, N
Porosity, ϕ (–)	0.25	0.35	0.1
Permeability, k (m^2)	10^{-17}	10^{-12}	5.0
Diffusion coefficient, D (m^2 s^{-1})[a]	10^{-12}	10^{-9}	3.0

[a]Defined as the ratio between the molecular diffusion coefficient of the salt in water by the tortuosity, which is obtained by the product of the formation factor with the connected porosity.

injection/abstraction of water (in s^{-1}). The effect of the salt concentration on the mass density and viscosity are neglected. In the so-called Fickian model, the hydrodynamic dispersion tensor is described by

$$\mathbf{D} = \left[\frac{D_m}{F\phi} + \alpha_T v\right]\mathbf{I}_3 + \frac{\alpha_L - \alpha_T}{v}\mathbf{v}\otimes\mathbf{v}, \tag{23}$$

where D_m is the molecular (mutual) diffusion coefficient of the salt (in m^2 s^{-1}; for a NaCl solution, D_m is 1.60×10^{-9} m^2 s^{-1} at infinite dilution and 1.44×10^{-9} m^2 s^{-1} at high salinities at 25 °C), $\boldsymbol{I}_3$ is the unit 3×3 tensor, $v = |\mathbf{v}|$, $\mathbf{a}\otimes\mathbf{b}$ represents the tensorial product between two vectors $\mathbf{a}$ and $\mathbf{b}$, α_L and α_T are the longitudinal (along $\mathbf{v}$) and transverse (normal to $\mathbf{v}$) dispersivities (in m) and the product between the formation factor and the connected porosity represents the tortuosity of the pore space, which controls the macroscopic diffusion coefficient $D = D_m/F\phi$ (Revil 1999) where F is the formation factor.

The finite element model is composed primarily of a single rectangular domain (100 m long by 20 m deep) defined as a function of the porosity ϕ, permeability k and molecular diffusion coefficient D (see Table 1). The longitudinal and transversal dispersivities will be considered constants.

The in-phase and out-of-phase (quadrature) surface conductivities are determined from the model developed by Revil & Florsch (2010) and Revil & Skold (2011). The mean grain diameter d_0 is computed from the permeability and the porosity $d_0 = (24F^3k)^{0.5}$ and $F = \phi^{-1.5}$ (Revil & Florsch 2010). The salinity dependence of Σ_S is taken into account using the model developed by Revil & Florsch (2010, their fig. 12). Longitudinal α_L and transverse α_T dispersivities are related as $\alpha_T = 0.2 - 0.01\alpha_L$, where α_L is commonly assumed between 0.01 and 0.1 m (Bear 1972). For our simulation, we use $\alpha_L = 1$ cm and $\alpha_T = 0.1$ cm. The effect of the salinity upon the electrical conductivity of the brine σ_f is accounted for by using the Sen & Goode (1992) model, which is valid from dilute concentrations to saturation in salt. When the induced polarization response is given by the model described in Revil & Florsch (2010) and when the surface conductivity term is small with respect to the pore water conductivity in the in-phase conductivity, the in-phase and quadrature conductivities are independent on the conductivity of the diffuse layer and the in-phase conductivity is nearly frequency independent.

A pressure differential is established across the domain by setting Dirichlet conditions at the inlet and outlet boundaries. The steady-state flow condition is on the order of $u = 0.1$ m s^{-1} across the domain. The geometry is shown in Fig. 11. The injection of a high salinity brine $\rho_f C^0_m = 500$ kg m^{-3} (salt saturation of the solution, 1000 times the background salinity of 0.5 kg m^{-3}) is simulated for duration of 7 min in an upstream well at a bottom hole depth of 5 m (Fig. 12). The total resultant flux of the salt within the model is simulated for 60 min. The resultant synthetic data comprises the transient amplitude and phase of the complex conductivity response computed at 1 Hz (Fig. 12). These data are inverted using the time-lapse ATC technique as described in Section 3.

5.2 Modelling and inversion results

The inversion results are shown in Figs 13 and 14. We consider 48 electrodes with 2 m spacing forming a total of 1422 dipole–dipole measurements per time-lapse data set. We assume that the time needed to take the data is short with respect to the characteristic

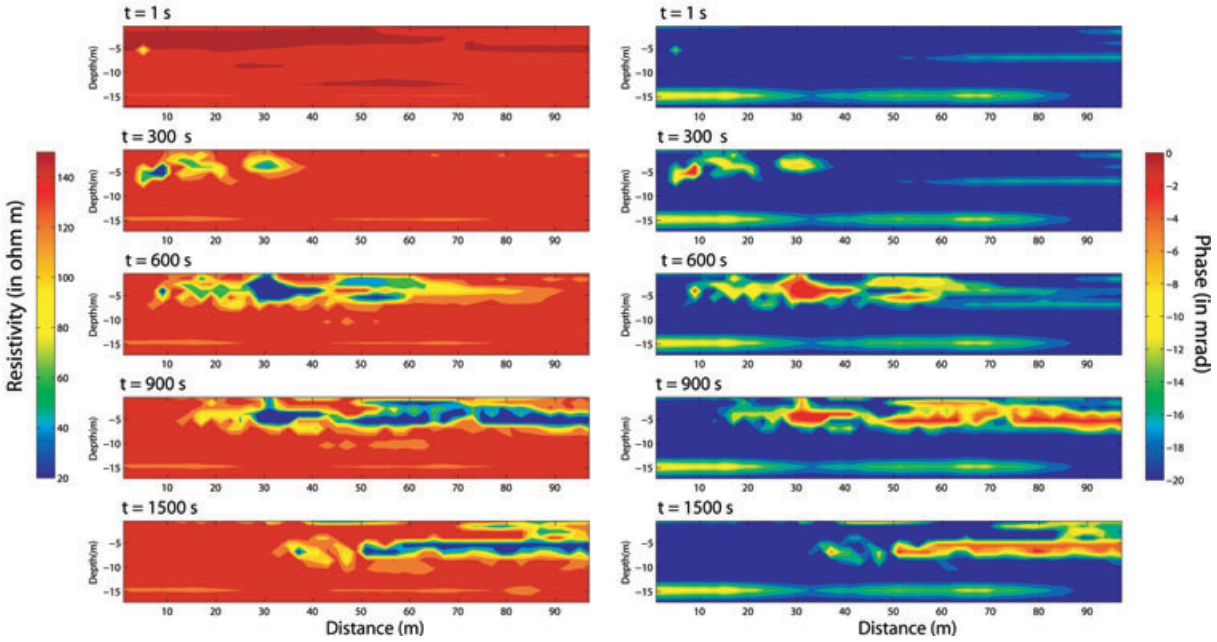


Figure 12. Result from the forward finite element modelling of the salt tracer test in terms of resistivity and phase at five different time steps (five snapshots). The phase accounts for both the effect of the resistivity and the influence of the salinity upon the quadrature conductivity through the dependence of the Stern layer surface conductivity on the salinity. The injection point for the salt is located at $x = 5$ m and $z = -5$ m.

Downloaded from https://academic.oup.com/gji/article/187/1/237/561878 by guest on 02 March 2021

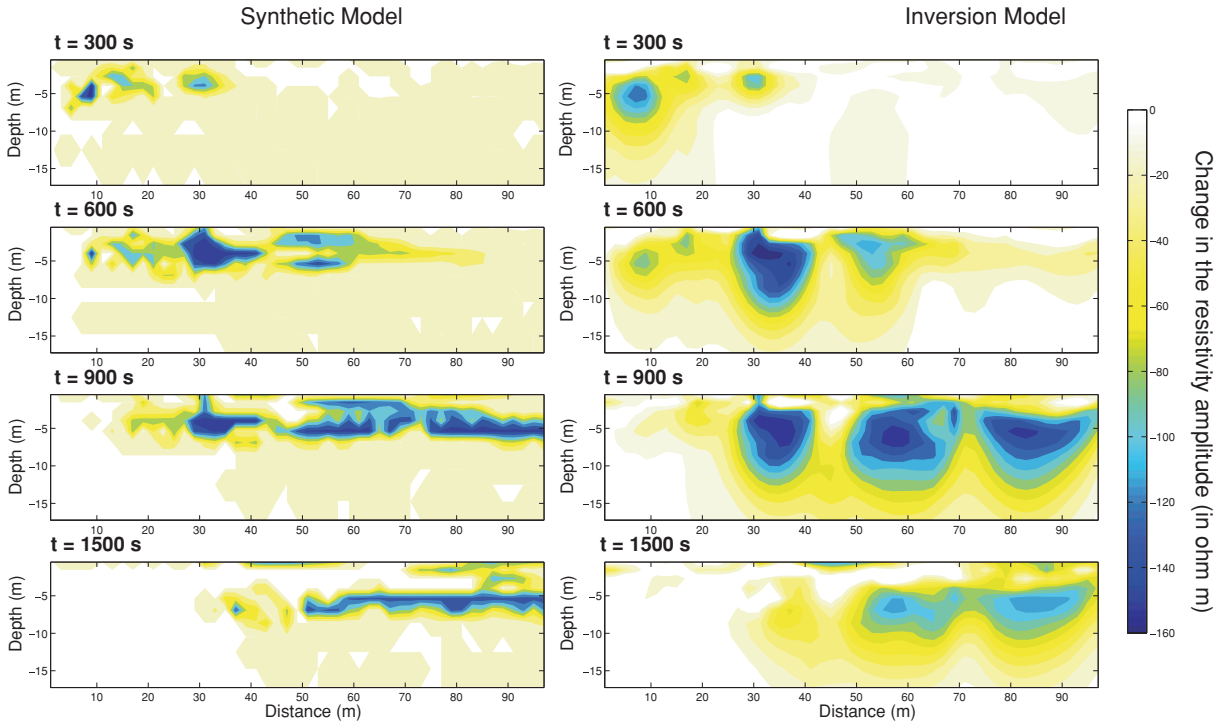


Figure 13. Comparison between the true resistivity changes from the forward model and the resistivity changes resulting from the time-lapse inversion of the apparent resistivity data collected from the top surface of the aquifer and contaminated with some noise. The results of the inversion are biased because we have assumed no prior knowledge of the anisotropy of the resistivity distribution of the medium.

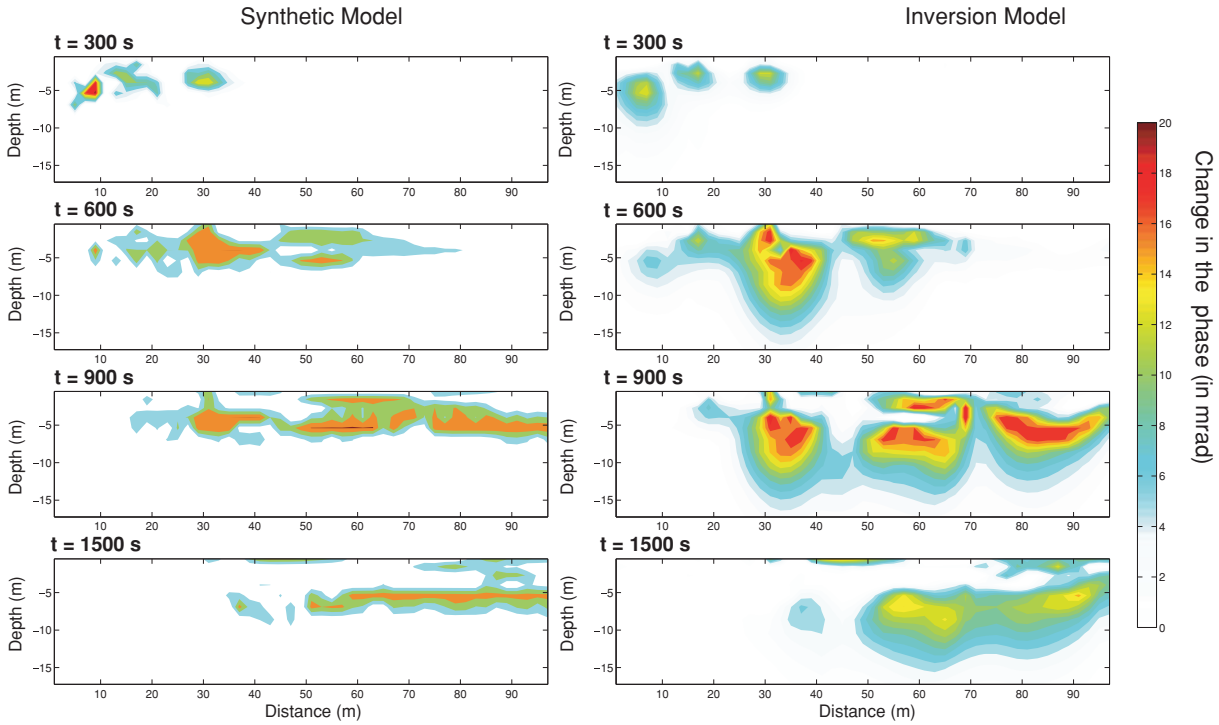


Figure 14. Comparison between the true changes of the phase (from the forward modelling associate with the simulation of the salt dispersion/advection problem) and the changes in the phase resulting from the time-lapse inversion of the apparent resistivity data and phase lags collected at the surface of the aquifer and contaminated with noise. The results of the inversion are biased because we have assumed no prior knowledge of the anisotropy of the resistivity distribution of the medium.

Downloaded from https://academic.oup.com/gji/article/187/1/237/561873 by guest on 02 March 2021

time associated with the transport of the salt (true snapshots). In the field, the duration of an acquisition is not necessarily small with respect to the resistivity changes and this limitation will need to be investigated in a future work. The data rms error for the time-lapse data set (difference between observed and calculated data) after five iterations was approximately 6 per cent. Model rms error varied from 6 to 70 per cent, depending on the complexity of the true model. It is important to note that the model rms error in a stochastically generated model is expected to have high values, similarly to real data, because no inversion scheme can find both the actual values of amplitude and phase in each cell. This being said, the tomograms compare fairly well with the true resistivity and phase distribution both in correctly localizing the anomalies and reproducing the amplitudes. Note that the shape of the resistivity and phase anomalies is, however, not completely reproduced, mainly because the stochastic model uses quite anisotropic distributions of the permeability and porosity (i.e. a much larger correlation length in the horizontal direction than in the vertical direction). In turn, this implies that the change in brine concentration is also quite anisotropic. It is likely that better results could be achieved if a borehole would be used to assess the correlation length for the vertical resistivity distribution and this information would be used in the cost function.

6 CONCLUSIONS

The independent inversion of time-lapse induced polarization data may produce significant errors because of both errors in the measurements and errors in the inversion. These errors can lead to misleading interpretations of the monitored process. The 4-D-ATC approach presented above reduces these errors, although allowing relatively abrupt resistivity time-related changes in the areas where there are significant indications of these changes. It removes a good fraction of the artefacts associated with noise in the data that is uncorrelated over time. The 4-D-ATC algorithm requires a pre-estimation of the position of the changing area. A method to estimate where those changes occur is to use the difference in the tomograms obtained from the independent inversions of the measurements at each time step. It may be useful to use higher-order time-related regularizations in the 4-D-ATC scheme. Numerical tests show that our approach works well on both a simple 3-D synthetic case study and on a 2-D simulation of a salt tracer transport in a heterogeneous synthetic aquifer. It is important to note, that although inversion convergence was in all cases less than 5 per cent, the model misfit is always larger. This observation is due the fact that inversion is an ill-posed problem and we cannot expect to find the exact complex conductivity values in each cell. In our work, the following assumptions were made: (i) the material properties vary linearly in time between two subsequent reference models, (ii) the acquisition time of a single time step is neglected (the time considered to take a snapshot is instantaneous, which for SIP data acquisition is generally untrue) and (iii) the effect of the salt concentration on the mass and viscosity were neglected in the second numerical test.

It could be interesting to perform a joint inversion of complex resistivity data with the self-potential data for salt tracer injection tests. Self-potential monitoring has been shown recently to be very useful to follow salt tracer tests (Martínez-Pagán *et al.* 2010; Revil & Jardani 2010). However, the inversion of self-potential data is an ill-posed and underdetermined geophysical problem too. Because the sensitivity maps of self-potential and induced polarization data are however quite different, these two types of geophysical data are naturally suited for a joint inversion problem to better follow salt tracer tests and then to use the results to invert the permeability and dispersivity tensor distributions in the subsurface.

ACKNOWLEDGMENTS

We thank Office of Science (BER), US. Department of Energy (Grant No. DE-FG02–08ER646559), NSF (SmartGeo Educational Program, Project IGERT: Intelligent Geosystems; DGE-0801692) and the U.S.EPA (Student Service Contract #EP10D00437) for financial supports. Although this work was reviewed by U.S.EPA and approved for presentation, it may not necessarily reflect official Agency policy. Mention of trade names or commercial products does not constitute endorsement or recommendation by U.S.EPA for use. We gratefully acknowledge fruitful discussions with Roland Martin (Bonn University) regarding the extension and testing of the inversion algorithm to the complex case. We thank Joerg Renner and two referees for their useful comments.

REFERENCES

Atekwana, E.A. *et al.*, 2004. Evidence for microbial enhanced electrical conductivity in hydrocarbon-contaminated sediments, *Geophys. Res. Lett.,* **31,** L23501, doi:10.1029/2004GL021359.

Bear, J., 1972. *Dynamics of Fluids in Porous Media,* Elsevier, New York, NY, 764pp.

Binley, A., Henry-Poulter, S. & Shaw, B., 1996. Examination of solute transport in an undisturbed soil column using electrical resistance tomography, *Water Resour. Res.,* **32,** 763–769.

Binley A., Slater L., Fukes, M. & Cassiani G., 2005. The relationship between frequency dependent electrical conductivity and hydraulic properties of saturated and unsaturated sandstone, *Water Resour. Res.,* **41**(12), W12417, doi:10.1029/2005WR004202.

Börner, F., Gruhne, M. & Schön J., 1993. Contamination indications derived from electrical properties in the low frequency range, *Geophys. Prospect.,* **41,** 83–98.

Börner, F.D., Schopper, W. & Weller, A., 1996. Evaluation of transport and storage properties in the soils and groundwater zone from induced polarization measurements, *Geophys. Prospect.,* **44,** 583–601, doi:10.1111/j.1365-2478.1996.tb00167.x.

Daily, W. & Ramirez, A.L., 2000. Electrical imaging of engineered hydraulic barriers, *Geophysics,* **65,** 83–94.

Daily, W., Ramirez, A., LaBrecque, D. & Nitao, J., 1992. Electrical resistivity tomography of vadose water movement, *Water Resour. Res.,* **28,** 1429–1442.

de Lima, O.A.L. & Sharma, M.M., 1992. A generalized Maxwell–Wagner theory for membrane polarization in shaly sands, *Geophysics,* **57,** 431–440.

Dey, A. & Morrison, H.F., 1979. Resistivity modeling for arbitrarily shaped three-dimensional structures, *Geophysics,* **44,** 753–780.

Flores Orozco, A., Williams, K.H., Long, P.E., Hubbard, S.S. & Kemna, A., 2011. Using complex resistivity imaging to infer biogeochemical processes associated with bioremediation of a uranium-contaminated aquifer, *J. geophys. Res.,* **116,** G03001, doi:10.1029/2010JG001591.

Florsch, N., Llubes, M., Téreygeol, F., Ghorbani, A. & Roblet, P., 2010. Quantification of slag heap volumes and masses through the use of induced polarization: application to the Castel-Minier site, *J. Archaeol. Sci.,* **38**(2), 438–451, doi:10.1016/j.jas.2010.09.027.

Ghorbani, A., Camerlynck C., Florsch N., Cosenza P., Tabbagh, A. & Revil A., 2007. Bayesian inference of the Cole-Cole parameters from time and frequency-domain induced polarization, *Geophys. Prospect.,* **55**(4), 589–605, doi:10.1111/j.1365-2478.2007.00627.x.

Hördt, A., Blaschek, R., Kemna, A. & Zisser, N., 2007. Hydraulic conductivity estimation from induced polarisation data at the field scale—the Krauthausen case history, *J. appl. Geophys.,* **62,** 33–46.

Downloaded from https://academic.oup.com/gji/article/187/1/237/561878 by guest on 02 March 2021

Karaoulis, M., Kim, J.-H. & Tsourlos, P.I., 2011. 4D active time constrained inversion, *J. appl. Geophys.,* **73,** 25–34.

Kemna, A., 2000. Tomographic inversion of complex resistivity-theory and application, *PhD thesis*, Ruhr-University of Bochum.

Kemna, A. & Binley, A., 1996. Complex electrical resistivity tomography for contaminant plume delineation, in *Proceedings of the 2nd Meeting on Environmental and Engineering Geophysics,* Environ. Eng. Geophys. Soc., Eur. Section, Nantes, pp. 196–199.

Kemna, A., Rakers, E. & Dresen, L., 1999. Field applications of complex resistivity tomography, *69th Annual International Meeting,* SEG Expanded Abstracts, pp. 331–334.

Kemna, A., Binley, A., Ramirez, A. & Daily, W., 2000. Complex resistivity tomography for environmental applications, *Chem. Eng. J.,* **77,** 11–18.

Kemna A., Binley, A. & Slater L., 2004. Crosshole IP imaging for engineering and environmental applications, *Geophysics,* **69(**1), 97–101.

Kim J.-H., Yi, M.J., Park, S.G. & Kim, J.G., 2009. 4-D inversion of DC resistivity monitoring data acquired over a dynamically changing earth model, *J. appl. Geophys.,* **68**(4), 522–532.

LaBrecque, D.J. & Yang, X., 2001. Difference inversion of ERT data: a fast inversion method for 3-D in situ monitoring, *J. Environ. Eng. Geophys.,* **5,** 83–90.

Legaz, A., Vandemeulebrouck J., Revil A., Kemna A., Hurst A.W., Reeves, R. & Papasin, R., 2009. A case study of resistivity and self-potential signatures of hydrothermal instabilities, Inferno Crater Lake, Waimangu, New Zealand, *Geophys. Res. Lett.,* **36,** L12306, doi:10.1029/2009GL037573.

Leroy, P. & Revil A., 2009. Spectral induced polarization of clays and clay-rocks, *J. geophys. Res.,* **114,** B10202, doi:10.1029/2008JB006114.

Leroy, P., Revil, A., Kemna, A., Cosenza, P. & Gorbani A., 2008. Spectral induced polarization of water-saturated packs of glass beads, *J. Coll. Interface Sci.,* **321**(1), 103–117.

Lesmes, D.P. & Morgan F.D., 2001. Dielectric spectroscopy of sedimentary rocks, *J. geophys. Res.,* **106**(B7), 13 329–13 346.

Looms, M.C., Jensen, K.H., Binley, A. & Nielsen, L., 2008. Monitoring unsaturated flow and transport using cross-borehole geophysical methods, *Vadose Zone J.,* **7,** 227–237.

Loke, M.H., Chambers, J.E. & Ogilvy, R.D., 2006. Inversion of 2D spectral induced polarization imaging data, *Geophys. Prospect.,* **54**, 287–301.

Martínez-Pagán P., Jardani A., Revil A. & Haas A., 2010. Self-potential monitoring of a salt plume, *Geophysics,* **75**(4), WA17–WA25, doi:10.1190/1.3475533.

Müller, K., Vanderborght, J., Englert, A., Kemna, A., Huisman, J.A., Rings, J. & Vereecken, H., 2010, Imaging and characterization of solute transport during two tracer tests in a shallow aquifer using electrical resistivity tomography and multilevel groundwater samplers, *Water Resour. Res.,* **46,** W03502. doi:10.1029/2008WR007595.

Nimmer, R.E., Osiensky, J.L., Binley, A.M., Sprenke, K.F. & Williams, B.C., 2007. Electrical resistivity imaging of conductive plume dilution in fractured rock, *Hydrogeol. J.,* **5,** 877–890.

Nguyen, F. *et al*., 2009. Characterization of seawater intrusion using 2D electrical imaging, *Near-Surf. Geophys.,* **7**(5–6), 377–390.

Nordsiek, S. & Weller, A., 2008. A new approach to fitting induced polarization spectra, *Geophysics,* **73,** F235–F245, doi:10.1190/1.2987412.

Ogilvy, R.D. *et al*., 2009. Automated time-lapse electrical resistivity tomography (ALERT) for monitoring coastal aquifers. *Near Surf. Geophys.,* **7**(5–6), 367–375.

Oldenburg, D.W., McGillivray, P.R. & Ellis, R.G., 1993. Generalized subspace methods for large-scale inverse problems, *Geophys. J. Int.,* **114,** 12–20.

Olhoeft, G.R., 1985. Low-frequency electrical properties, *Geophysics,* **50,** 2492–2503.

Olhoeft, G.R., 1986. Direct detection of hydrocarbon and organic chemicals with ground-penetrating radar and complex resistivity, *Proceedings of the NWWA/API Conference on Petroleum Hydrocarbons and Organic Chemicals in Ground Water-Prevention, Detection, and Restoration,* 1985 November 13–15, Houston, TX, pp. 284–305.

Park, S., 1998. Fluid migration in the vadose zone from 3-D inversion of resistivity monitoring data, *Geophysics,* **63**(1), 41–51.

Pelton, W.H., Ward, S.H., Hallof, P.G., Sill, W.R. & Nelson, P.H., 1978. Mineral discrimination and removal of inductive coupling with multifrequency IP, *Geophysics,* **43,** 588–609.

Ramirez, A., Daily, W., LaBrecque, D., Owen, E. & Chesnut, D., 1993. Monitoring an underground steam injection process using electrical resistance tomography, *Water Resour. Res.,* **29,** 73–87.

Revil A., 1999. Ionic diffusivity, electrical conductivity, membrane and thermoelectric potentials in colloids and granular porous media: a unified model, *J. Coll. Interface Sci.,* **212,** 503–522.

Revil, A. & Jardani, A., 2010. Stochastic inversion of permeability and dispersivities from time lapse self-potential measurements: a controlled sandbox study, *Geophys. Res. Lett.,* **37,** L11404, doi:10.1029/2010GL043257.

Revil, A. & Florsch, N., 2010. Determination of permeability from spectral induced polarization data in granular media, *Geophys. J. Int.,* **181,** 1480–1498, doi:10.1111/j.1365-246X.2010.04573.x.

Revil, A. & Skold, M., 2011. Salinity dependence of spectral induced polarization in sands and sandstones, *Geophys. J. Int.,* in press, doi:10.1111/j.1365-246X.2011.05184.x.

Revil, A., Cathles, L.M., Losh, S. & Nunn, J.A., 1998. Electrical conductivity in shaly sands with geophysical applications, *J. geophys. Res.,* **103**(B10), 23 925–23 936.

Routh, P.S., Oldenburg, D.W. & Li, Y., 1998. Regularized inversion of spectral IP parameters from complex resistivity data, *68th Annual International Meeting,* SEG, Expanded Abstracts, pp. 810–813.

Seigel, H., Nabighian, M., Parasnis, D.S. & Vozoff, K., 2007. The early history of the induced polarization method, *Leading Edge,* **3,** 312–321.

Sen, P.N. & Goode, P.A., 1992. Influence of temperature on electrical conductivity on shaly sands, *Geophysics,* **57,** 89–96.

Schmutz, M., Revil, A., Vaudelet, P., Batzle, M., Femenía Viñao, P. & Werkema, D. D. Influence of oil saturation upon spectral induced polarization of oil bearing sands, *Geophys. J. Int.,* **183,** 211–224, doi:10.1111/j.1365-246X.2010.04751.x.

Shi, W., Rodi, W. & Morgan, F.D., 1998. 3-D induced polarization inversion using complex electrical resistivities, in *Proceedings of the Symposium on Application of Geophysics to Engineering and Environmental Problems*, Environ. Eng. Geophys. Soc., Chicago, IL, pp. 785–794.

Singha, K. & Gorelick, S.M., 2005. Saline tracer visualized with electrical resistivity tomography: field scale spatial moment analysis, *Water Resour. Res.,* **41,** W05023, doi:10.1029/2004WR003460.

Slater, L., Binley, A.M., Versteeg, R., Cassiani, G., Birken, R. & Sandleberg, S., 2002. A 3D ERT study of solute transport in a large experimental tank, *J. appl. Geophys.,* **49,** 211–229.

Tsourlos, P. & Ogilvy R., 1999. An algorithm for the 3-D inversion of topographic resistivity and induced polarization data: preliminary results, *J. Balkan geophys. Soc.,* **2**(2), 30–45.

Vanhala, H., 1997. Mapping oil-contaminated sand and till with the spectral induced polarization (SIP) method, *Geophys. Prospect.,* **45,** 303–326.

Vaudelet, P., Revil, A., Schmutz, M., Franceschi, M. & Bégassat, P., 2011a. Induced polarization signature of the presence of copper in saturated sands, *Water Resour. Res.,* **47,** W02526, doi:10.1029/2010WR009310.

Vaudelet, P., Revil, A., Schmutz, M., Franceschi, M. & Bégassat, P., 2011b. Changes in induced polarization associated with the sorption of sodium, lead, and zinc on silica sands, *J. Coll. Interface Sci.,* **360,** 739–752.

Waxman, M.H. & Smits, L.J.M., 1968. Electrical conductivities in oil-bearing sands, *Soc. Pet. Eng. J.,* **8,** 107–122.

Weller, A., Seichter, M. & Kampke, A., 1996. Induced-polarization modeling using complex electrical conductivities, *Geophys. J. Int.,* **127,** 387–398.

Williams, K.H. *et al*., 2009. Geophysical monitoring of coupled microbial and geochemical processes during stimulated subsurface bioremediation, *Environ. Sci. Technol.,* **43,** 6717–6723, doi:10.1021/es900855j.

Yi, M.J., Kim, J.H. & Chung, S.H., 2003. Enhancing the resolving power of least-squares inversion with active constraint balancing, *Geophysics,* **68,** 931–941.

Zhang, Y., Ghodrati, A. & Brooks, D.H., 2005. An analytical comparison of three spatio-temporal regularization methods for dynamic linear inverse problems in a common statistical framework, *Inverse Problems,* **21,** 357–382.

Downloaded from https://academic.oup.com/gji/article/187/1/237/561873 by guest on 02 March 2021